Power Balance in Aerodynamic Flows

Mark Drela

MIT Dept. of Aeronautics and Astronautics, Cambridge, MA, 02139

Abstract

A control volume analysis of the compressible viscous flow about an aircraft is performed, including integrated propulsors and flow control systems. In contrast to most past analyses which have focused on forces and momentum flow, in particular thrust and drag, the present analysis focuses on mechanical power and kinetic energy flow. The result is a clear identification and quantification of all the power sources, power sinks, and their interactions which are present in any aerodynamic flow. The formulation does not require any separate definitions of thrust and drag, and hence it is especially useful for analysis and optimization of aerodynamic configurations which have tightly integrated propulsion and boundary layer control systems.

Nomenclature

ρ, μ	fluid density, viscosity
b, c	wing span and chord
p, p_t	static pressure, total pressure
$\hat{n}$	unit normal vector, out of control volume
t	time
u, v, w	perturbation velocities
u, w	shear layer velocities (in shear layer section)
x, y, z	cartesian axes
$\vec{V}$	fluid velocity $(= (V_\infty + u)\hat{x} + v\hat{y} + w\hat{z})$
V^2	fluid speed squared $(= \vec{V} \cdot \vec{V})$

V_n	Side Cylinder normal velocity ($= vn_y + wn_z$)
$\bar{\bar{\tau}}$	viscous stress tensor
$\vec{\tau}$	surface viscous stress vector ($= \bar{\bar{\tau}} \cdot \hat{n}$)
C_f	skin friction coefficient
$C_{\mathcal{D}}$	dissipation coefficient
H	boundary layer shape parameter ($= \delta^*/\theta$)
H^*	kinetic energy shape parameter ($= \theta^*/\theta$)
$\theta\,, \delta^*$	momentum, displacement thicknesses
θ^*, δ^{**}	kinetic energy, density-flux thicknesses
δ_{κ}	wake kinetic energy excess thickness
Re_θ	mom. thickness Reynolds number ($= u_e\theta/\nu$)
Re_c	chord Reynolds number ($= V_\infty c/\nu$)
$\dot{m}$	mass flow
F_x, F_z	total streamwise, normal aerodynamic forces
F_u	streamwise force from axial velocity u
F_v	streamwise force from transverse velocities v, w
F_n	streamwise force from lateral outflow velocity V_n
D_p	profile drag
D_i	induced drag
D_w	wave drag
$\dot{E}_{\mathrm{a}}$	axial kinetic energy deposition rate
$\dot{E}_{\mathrm{v}}$	transverse (vortex) kinetic energy deposition rate
$\dot{E}_{\mathrm{p}}$	pressure-work deposition rate
$\dot{E}_{\mathrm{w}}$	lateral wave-outflow energy deposition rate
$P_{\mathcal{S}}$	shaft power
$P_{\mathcal{V}}$	volumetric power

P_K kinetic energy inflow rate

T thrust

$\dot{\mathcal{E}}$ mechanical energy outflow rate

Φ dissipation rate

Γ airfoil circulation

$d\mathcal{S}$ surface element of control volume

$d\mathcal{V}$ volume element of control volume

W aircraft weight

γ climb angle

$\dot{h}$ climb rate ($= V_\infty \sin\gamma$)

Subscripts

$()_\infty$ freestream quantity

$()_B$ quantity on body surface

$()_O$ quantity on outer boundary

$()_O^{SC}$ quantity on Side Cylinder

$()_O^{TP}$ quantity on Trefftz Plane

$()_e$ shear layer edge quantity

1 Introduction

Numerous previous workers have analyzed the flow about an aerodynamic body via a Control Volume approach, in order to relate the body forces to the wake and the flow farfield. The early work of Betz [1], Jones [2] and Oswatisch [3] focused on drag, while Maskell [4] considered both lift and drag for incompressible flow, and Kroo [5] reviewed various techniques for induced drag prediction and reduction. The recent efforts

of VanDam [6], Giles and Cummings [7], and Kusunose [8] have treated the general compressible case, also with enthalpy addition from engines. More recently, Méheut and Bailly [9] have done an overview and comparison of most of the previous analyses and approaches for the drag component, and introduce their own refinement. Spalart [10] performs an even more detailed analysis for the incompressible case using inner and outer expansions of the far wake, and identifies a higher-order farfield term in the overall axial force which has been previously neglected.

The goals of the previous developments have been to allow accurate wind tunnel drag measurements from wake surveys, with or without wind tunnel wall interference, and also to allow accurate drag computation from CFD results despite the presence of imperfect freestream boundary conditions and numerical errors. Additional benefits have been the clear identification of drag-producing sources in the flow, and relation of experiments and CFD results to other classical analyses such as lifting-line theory.

All the previous work has focused almost exclusively on momentum-equation analysis, giving relations for the aerodynamic lift and drag forces. The implied propulsive power was then simply defined to be drag $\times$ velocity. Thermodynamic and state relations were also introduced, but only as a means to relate velocity and pressure to enthalpy and entropy in the downstream wake. In contrast, the present analysis will begin with the mechanical-energy equation from the outset, giving relations between mechanical power and dissipation in the flowfield. The result is especially applicable for evaluation of complex aerodynamic configurations, especially ones with tightly-integrated propulsion and boundary layer control systems.

It is worthwhile here to mention related work done for turbomachinery applications. Denton and Cumpsty [11] and also Denton [12] examined the dissipation and associated entropy and loss generation mechanisms on turbomachinery blading, wakes, and tip gaps. Greitzer et al [13] also did an overview and further analyses of various flow situations. In the context of the present work, the previous turbomachinery work would be particularly relevant for estimating the losses of flow control systems and associated ducts and impellers.

2 Control Volume Definition

Figure 1 shows the Control Volume (CV) surrounding the flow around an aerodynamic body. The CV boundary $\mathcal{S}$ is partitioned into an inner boundary $\mathcal{S}_B$ lying on the body surface, and an outer boundary $\mathcal{S}_O$ lying in the flowfield. Together with Gauss's Theorem we therefore have

$$\begin{aligned} \iiint \nabla\cdot(\ )\ d\mathcal{V} &= \oiint (\ )\cdot\hat{n}\ d\mathcal{S} \\ &= \oiint (\ )\cdot\hat{n}\ d\mathcal{S}_B + \oiint (\ )\cdot\hat{n}\ d\mathcal{S}_O \end{aligned} \tag{1}$$

where ( ) is any field vector quantity. The outer boundary $\mathcal{S}_O$ portions will be assumed to be oriented so that

1a) The downstream Trefftz Plane portion $\mathcal{S}_O^{TP}$ is oriented perpendicular to $\vec{V}_\infty$, and

1b) The Side Cylinder portion $\mathcal{S}_O^{SC}$ is parallel to $\vec{V}_\infty$.

These restrictions will considerably simplify most of the integral expressions to be derived.

The distance to the outer boundaries is completely arbitrary. However, it will be highly advantageous to place them so that

2a) All vortical fluid leaves via $\mathcal{S}_O^{TP}$, while any supersonic oblique waves which are present leave via $\mathcal{S}_O^{SC}$, and

2b) The distance to the Side Cylinder is at least several times the wing span of the configuration.

Unlike 1a) and 1b), these 2a) and 2b) are not hard requirements, but they do bring the great advantage of isolating different physical flow processes in separate terms in the equations.

3 Periodic-Unsteady Treatment

The present work will address steady or periodic-unsteady aerodynamic flows. The latter case must be addressed, because mechanical propulsors, impellers, or even flapping wings are treated as part of the

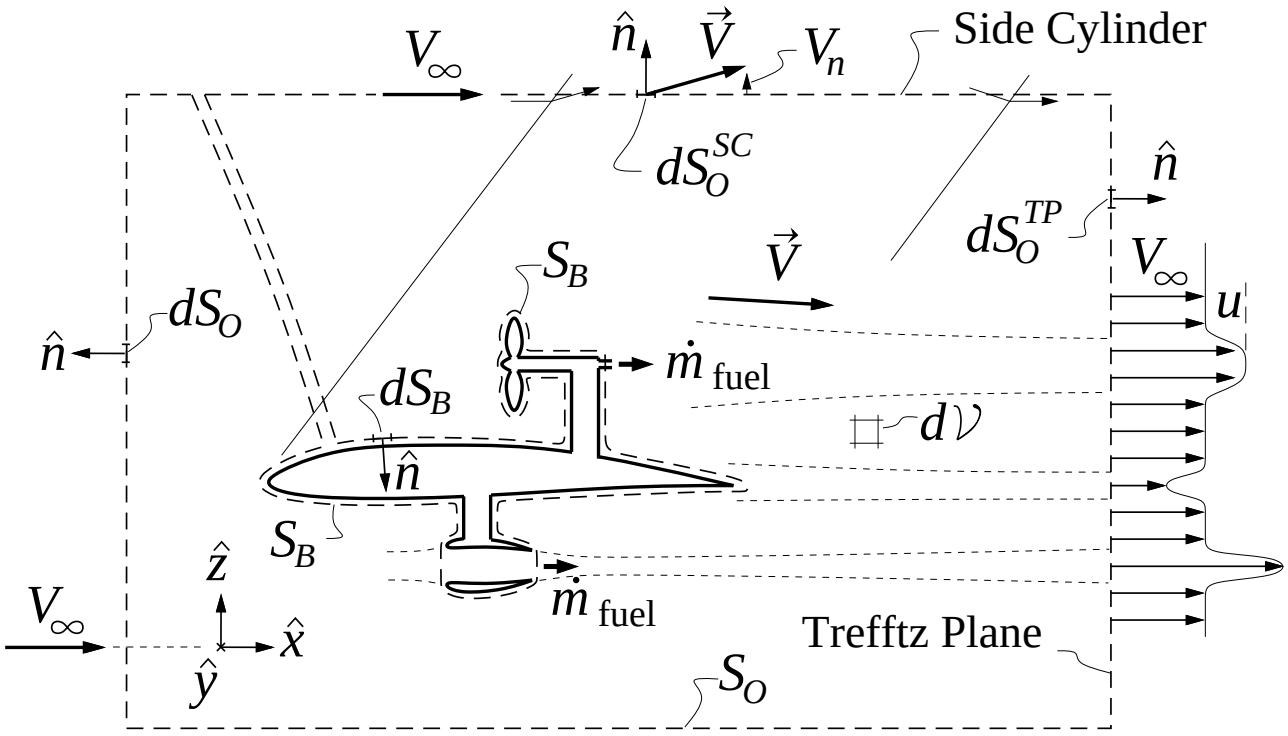

Figure 1: 2D cutaway view of 3D Control Volume surrounding an aerodynamic body. The inner boundary $\mathcal{S}_B$ lies on the body, and may cover moving elements (top propulsor), or hide them inside (bottom propulsor). Vortex-wake velocities v, w on Trefftz Plane are not shown.

flowfield. Their periodic unsteadiness produces nonzero nonlinear-term contributions to the time-averaged flow.

Consider the periodic unsteady velocity components $\tilde{u}, \tilde{v}$, which can be expanded about their mean values $\bar{u}, \bar{v}$ in the form

$$\tilde{u}(x,y,z,t) \;=\; \bar{u}(x,y,z) + \sum_{k=1}^{\infty} u_k(x,y,z)\, \sin\frac{2\pi k t}{t_\mathrm{p}} \tag{2}$$

$$\tilde{v}(x,y,z,t) \;=\; \bar{v}(x,y,z) + \sum_{k=1}^{\infty} v_k(x,y,z)\, \sin\frac{2\pi k t}{t_\mathrm{p}} \tag{3}$$

where t_p is the period. Time-averaging the velocities and their quadratic products then gives

$$u(x,y,z) \;\equiv\; \frac{1}{t_\mathrm{p}} \int_0^{t_\mathrm{p}} \tilde{u}\, dt \;=\; \bar{u} \tag{4}$$

$$uv(x,y,z) \;\equiv\; \frac{1}{t_\mathrm{p}} \int_0^{t_\mathrm{p}} \tilde{u}\tilde{v}\, dt \;=\; \bar{u}\bar{v} + \sum_{k=1}^{\infty} \tfrac{1}{2} u_k v_k \tag{5}$$

which mimics the Reynolds-averaging procedure for turbulent flows. Similar expressions can be obtained for cubic or higher products. Also, phase differences can be introduced by adding cosine-expansion sums, which will also result in additional coefficient-product sums.

In brief, product quantities such as "uv" imply the presence of unsteady-coefficient product sums such as $\sum \frac{1}{2} u_k v_k$, etc, which will be omitted for brevity in the expressions. These omitted sums are expected to be important only for cases with large-scale unsteadiness, such as flapping wings. For such cases, the missing sums can then always be added to the various CV quantity spatial integrands in order to obtain the exact time-average form.

4 Mass and Momentum Analysis

Although this work will focus primarily on a mechanical energy analysis, a brief mass and force analysis is necessary to simplify the later results.

4.1 Mass relation

The time-averaged mass continuity equation for fluid flow is as follows.

$$\nabla \cdot \left(\rho \vec{V} \right) \;=\; 0 \tag{6}$$

As described in the previous section, the unsteady-coefficient product sum $\sum \frac{1}{2} \rho_k \vec{V}_k$ is implicitly present inside the divergence, but has been omitted for clarity. Forming the volume integral $\iiint \{\text{equation (6)}\}\, d\mathcal{V}$ over the CV and invoking relation (1) then gives the following integral mass equation.

$$\boxed{\dot{m}_{\scriptscriptstyle B} \;=\; \dot{m}_{\scriptscriptstyle O}} \tag{7}$$

$$\dot{m}_{\scriptscriptstyle B} \;=\; -\oiint \rho \vec{V} \cdot \hat{n}\, d\mathcal{S}_{\scriptscriptstyle B} \;=\; \dot{m}_{\text{fuel}} \;\simeq\; 0 \tag{8}$$

$$\dot{m}_{\scriptscriptstyle O} \;=\; \oiint \rho \vec{V} \cdot \hat{n}\, d\mathcal{S}_{\scriptscriptstyle O} \;=\; \dot{m}_{\text{fuel}} \;\simeq\; 0 \tag{9}$$

These will be used only to manipulate and simplify other subsequent integral relations. As indicated, the fuel mass flow will be considered negligible.

4.2 Momentum and force relations

The time-averaged momentum equation in divergence form is as follows.

$$\nabla \cdot \left(\rho \vec{V} \, \vec{V} \right) \;=\; -\nabla p \,+\, \nabla \cdot \bar{\bar{\tau}} \tag{10}$$

Forming the volume integral $\iiint \{\text{equation (10)}\}\, d\mathcal{V}$ over the CV and invoking relation (1) then gives the integral momentum equation

$$\boxed{\vec{F}_{B} \;=\; \vec{F}_{O}} \tag{11}$$

where the following definitions have been made.

Net force on body, including propulsors:

$$\vec{F}_{B} \;=\; \oiint \Big[\left(p\,\hat{n} - \vec{\tau} \right) \,+\, \vec{V}\, \rho \vec{V} \cdot \hat{n} \Big]\, d\mathcal{S}_{B} \tag{12}$$

Outer-boundary force, momentum flow:

$$\vec{F}_{O} \;=\; \oiint -\Big[(p - p_{\infty})\, \hat{n} \,+\, \left(\vec{V} - \vec{V}_{\infty} \right) \rho \vec{V} \cdot \hat{n} \Big]\, d\mathcal{S}_{O} \tag{13}$$

In the $\vec{F}_{B}$ definition, the surface shear stress vector $\vec{\tau} = \bar{\bar{\tau}} \cdot \hat{n}$ has been introduced for convenience. In the $\vec{F}_{O}$ definition, p has been replaced with $p - p_{\infty}$, which is permissible because of the general relation

$$\oiint \hat{n}\, d\mathcal{S} \;=\; 0 \tag{14}$$

for any closed surface. Also, $\vec{V}$ has been replaced with $\vec{V} - \vec{V}_{\infty}$ which is permissible because of the mass relation (9).

The x-axis is now chosen to lie along the flight path. Then for steady unbanked flight at some climb angle γ, in a still atmosphere, we have

$$\vec{F}_{B} \;=\; \vec{F}_{O} \;=\; F_{x}\, \hat{x} \,+\, 0\, \hat{y} \,+\, F_{z}\, \hat{z} \tag{15}$$

$$-F_x \;=\; W\,\sin\gamma \tag{16}$$

$$F_z \;=\; W\,\cos\gamma \tag{17}$$

where F_x is the net streamwise aerodynamic force, F_z is the net normal aerodynamic force, and W is the weight. F_x will now be related to the outer-boundary integral in the $\vec{F}_O$ definition.

4.3 Streamwise Force Decomposition

With the Trefftz Plane and Side Cylinder boundaries defined perpendicular and parallel to $\vec{V}_\infty$, the streamwise x-component of the outer force (13) reduces to the following.

$$\boxed{\begin{aligned} F_x \;&=\; \iint -\Big[(p-p_\infty) \;+\; \rho u\,(V_\infty + u)\Big]\, d\mathcal{S}_O^{TP} \\ &\quad + \iint -\rho u\, V_n \; d\mathcal{S}_O^{SC} \end{aligned}} \tag{18}$$

To put the first integral above into a more convenient form for later use with the kinetic energy analysis, we make the exact substitution

$$V_\infty\, u \;=\; \tfrac{1}{2}\left(V^2 - V_\infty^2\right) \;-\; \tfrac{1}{2}\left(u^2+v^2+w^2\right) \tag{19}$$

which gives a natural decomposition of the net streamwise force into three components:

$$F_x \;=\; F_u \;+\; F_v \;+\; F_n \tag{20}$$

$$F_u \;= \iint \Big[(p_\infty - p) + \tfrac{1}{2}\rho\big(V_\infty^2 - V^2\big) - \tfrac{1}{2}\rho u^2\Big]\, d\mathcal{S}_O^{TP} \tag{21}$$

$$F_v \;= \iint \tfrac{1}{2}\rho\big(v^2+w^2\big)\; d\mathcal{S}_O^{TP} \tag{22}$$

$$F_n \;= \iint -\rho u\, V_n \, d\mathcal{S}_O^{SC} \tag{23}$$

The F_u component is the net "profile drag – thrust" force associated with the axial perturbation velocity u. For low speed flow and small $u \ll V_\infty$, it is effectively a total pressure defect

$$F_u \;\simeq \iint \Big[p_{t_\infty} - p_t\Big]\, d\mathcal{S}_O^{TP} \;-\; \mathcal{O}\big(\rho u^2\big) \tag{24}$$

whose integrand is negligible outside the viscous wakes and propulsion plumes. In contrast, the bulk of the F_v integrand in (22) comes from the trailing-vortex potential crossflow over the entire Trefftz Plane, and

hence is closely related to the induced drag D_i which will be discussed later. The remaining F_n term is zero for a sufficiently distant Side Cylinder in subsonic flow, and equal to the farfield wave drag D_w in supersonic flow which will also be discussed later.

In most force analyses of aircraft, F_u is typically separated into profile drag and thrust.

$$F_u \;=\; D_p - T \tag{25}$$

However, this decomposition is often ambiguous for aircraft whose propulsion system is closely integrated with the airframe, and for aircraft which employ powered lift or boundary layer control systems. It will be seen that in the present power-based analysis, decomposition (25) is entirely unnecessary.

Most of the previous workers mentioned in the Introduction have further manipulated the F_u expression into equivalent forms in terms of entropy and total enthalpy. The F_v or D_i expression has also been manipulated into an equivalent form in terms of the crossflow streamfunction and the streamwise vorticity. Here these alternative forms will not be used, since they are not particularly useful in the subsequent mechanical energy analysis.

5 Mechanical Energy Analysis

Forming the dot product {equation (10)}$\cdot\vec{V}$ gives the mechanical (kinetic) energy equation in divergence form.

$$\nabla \cdot \left(\rho \vec{V} \, \tfrac{1}{2} V^2 \right) \;=\; -\nabla p \cdot \vec{V} \;+\; (\nabla \cdot \bar{\bar{\tau}}) \cdot \vec{V} \tag{26}$$

Using the general vector identities

$$\nabla \cdot \left(p \vec{V} \right) \;=\; \nabla p \cdot \vec{V} \;+\; p \, \nabla \cdot \vec{V} \tag{27}$$

$$\nabla \cdot \left(\bar{\bar{\tau}} \cdot \vec{V} \right) \;=\; (\nabla \cdot \bar{\bar{\tau}}) \cdot \vec{V} \;+\; (\bar{\bar{\tau}} \cdot \nabla) \cdot \vec{V} \tag{28}$$

the right side of equation (26) is expanded as follows.

$$\nabla \cdot \left(\rho \vec{V} \, \tfrac{1}{2} V^2 \right) \;=\; -\nabla \cdot \left(p \vec{V} \right) \;+\; p \nabla \cdot \vec{V}$$

$$+ \quad \nabla\cdot\left(\bar{\bar{\tau}}\cdot\vec{V}\right) \; - \; (\bar{\bar{\tau}}\cdot\nabla)\cdot\vec{V} \tag{29}$$

We now form the integral $\iiint\{\text{equation (29)}\}\,d\mathcal{V}$ over the entire CV, and apply relation (1) to give the following integral mechanical power balance equation

$$\boxed{P_{_S} \; + \; P_{_V} \; + \; P_{_K} \;\; = \;\; \dot{\mathcal{E}} \; + \; \Phi} \tag{30}$$

where the five terms are defined below. The substitutions $p \to p - p_\infty$ and $V^2 \to V^2 - V_\infty^2$ have been made as in the momentum equation analysis.

The three terms on the left side of (30) represent the total mechanical power supply, production, or inflow, ultimately from fuel, batteries, or other source. The two terms on the right represent power consumption or outflow, via various physical processes. The balance holds instantaneously in steady flow, or as a period-average in unsteady periodic flow. A major goal of the present paper is the determination of the total power required for flight, via the prediction and estimation of the righthand side terms in equation (30) or its equivalents to be derived later.

Net propulsor shaft power:

$$\boxed{P_{_S} \;\; = \;\; \oiint\left[-(p-p_\infty)\,\hat{n} \; + \; \vec{\tau}\,\right]\cdot\vec{V}\;d\mathcal{S}_{_B}} \tag{31}$$

This is the integrated (force)·(velocity) on all moving body surfaces, and hence is the net total propulsor shaft power or wing-flapping power for all the components on the aircraft which are covered by the body control volume surface $\mathcal{S}_{_B}$. If individual turbomachinery component blading is defined to be covered by $\mathcal{S}_{_B}$, such as for the upper propulsor in Figure 1, then $P_{_S}$ will include positive contributions from a compressor, and negative contributions from a turbine. If the aircraft has powered lift or other boundary layer control systems whose impeller blades are covered by $\mathcal{S}_{_B}$, then $P_{_S}$ will also include the shaft power of the impellers.

Net pressure-volume "P dV" power:

$$\boxed{P_{_V} \;\; = \;\; \iiint (p-p_\infty)\,\nabla\cdot\vec{V}\;d\mathcal{V}} \tag{32}$$

This is a volumetric (or "P dV") mechanical power, provided by the fluid expanding against atmospheric pressure. Its integrand will have strong net contributions at locations wherever heat is added at a pressure far from ambient, for example if a turbomachinery combustor is chosen to be inside the CV, or if external combustion is present as in some hypersonic vehicles. In supersonic wave regions the P_V integrand may be nonzero, but will cancel when integrated over all points whose streamlines reversibly return to the freestream state before exiting the CV. Obtaining this cancellation is the main motivation behind defining the CV such that the wave system exits through the Side Cylinder, and ahead of the Trefftz Plane.

Net propulsor mechanical energy flow rate into the CV:

$$\boxed{P_K \;=\; \oiint \Big[(p-p_\infty) + \tfrac{1}{2}\rho\big(V^2-V_\infty^2\big)\Big]\vec{V}\cdot\hat{n}\; d\mathcal{S}_B} \tag{33}$$

This is the net pressure-work and kinetic energy flow rate across $\mathcal{S}_B$ and into the CV. This accounts for power sources whose moving blading is <u>not</u> covered by $\mathcal{S}_B$, or whose combustors are outside the CV, such as the bottom propulsor in Figure 1. Note that $\hat{n}$ points into the propulsor, so that the nozzle has $\vec{V}\cdot\hat{n} < 0$, and $P_K > 0$ for a propulsor with net thrust, as expected.

Mechanical energy flow rate out of the CV:

$$\boxed{\begin{aligned}\dot{\mathcal{E}} \;&=\; \iint \Big[(p-p_\infty) + \tfrac{1}{2}\rho\big(V^2-V_\infty^2\big)\Big](V_\infty+u)\; d\mathcal{S}_O^{TP} \\ &+\; \iint \Big[(p-p_\infty) + \tfrac{1}{2}\rho\big(V^2-V_\infty^2\big)\Big]\, V_n\; d\mathcal{S}_O^{SC}\end{aligned}} \tag{34}$$

This is the net pressure-work rate and kinetic energy flow rate out of the CV, through the Trefftz Plane and Side Cylinder boundaries.

Viscous dissipation rate:

$$\boxed{\Phi \;=\; \iiint (\bar{\bar{\tau}}\cdot\nabla)\cdot\vec{V}\; d\mathcal{V}} \tag{35}$$

This measures the rate at which kinetic energy of the flow is converted into heat inside the CV. The dissipation mechanism is the viscous stresses $\bar{\bar{\tau}}$ working against fluid deformation, the latter related to the velocity gradients $\nabla\vec{V}$. In practice, most of the dissipation occurs in the thin boundary layers on the aircraft surface, including the propulsion elements, and also in shock waves. If powered lift or boundary layer control

systems are present, then the air in the suction or blowing plumbing can be considered as part of the flowfield, and the dissipation inside the plumbing would contribute to the overall Φ. Additional dissipation also occurs in the downstream wakes and jets, as shown in Figure 2, and discussed later.

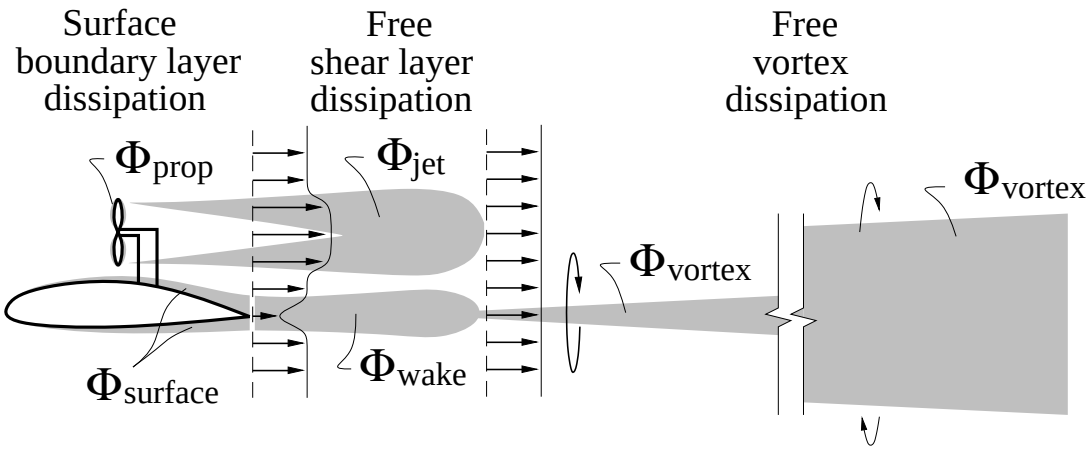

Figure 2: Dissipation in various flow regions inside the CV. Not shown is additional dissipation which may occur inside any flow control system ducting. Also not shown is dissipation in shock waves.

5.1 Energy outflow rate decomposition

The total energy rate $\dot{\mathcal{E}}$ definition (34) captures the outflow of all mechanical energy regardless of type or origin, making the power balance equation (30) somewhat difficult to apply and interpret. To clarify the situation, we now use the F_x definition (18), the weight relation (16), and the velocity relation (19), and exactly decompose $\dot{\mathcal{E}}$ into five separate components,

$$\dot{\mathcal{E}} \;=\; W\dot{h} + \dot{E}_{\rm a} + \dot{E}_{\rm v} + \dot{E}_{\rm p} + \dot{E}_{\rm w} \tag{36}$$

each of which has a relatively clear physical origin. The result is the following alternative and equivalent form of the integral power balance equation,

$$\boxed{P_{\scriptscriptstyle S} + P_{\scriptscriptstyle V} + P_{\scriptscriptstyle K} \;=\; W\dot{h} + \dot{E}_{\rm a} + \dot{E}_{\rm v} + \dot{E}_{\rm p} + \dot{E}_{\rm w} + \Phi} \tag{37}$$

where the five $\dot{\mathcal{E}}$ components are defined below.

Potential energy rate:

$$\boxed{W\dot{h} \;=\; -F_x V_\infty \;=\; W V_\infty \sin\gamma} \tag{38}$$

This is simply the power consumption needed to increase the aircraft's potential energy, and becomes a power source during descent. The decomposition (37) therefore isolates this reversible $\dot{\mathcal{E}}$ component, leaving the remaining four components to capture all the irreversible outflow losses.

Wake streamwise kinetic energy deposition rate:

$$\boxed{\dot{E}_{\mathrm{a}} \;=\; \iint \tfrac{1}{2}\rho\, u^2 \;(V_\infty + u)\; d\mathcal{S}_O^{TP}} \tag{39}$$

This is the rate of streamwise kinetic energy being deposited in the flow out of the CV, through the Trefftz Plane. Note that this is always positive, both in the case of a propulsive jet where the axial perturbation velocity u is positive, and also for a wake where u is negative (assuming no reverse flow in the Trefftz Plane, or $V_\infty + u > 0$).

Wake transverse kinetic energy deposition rate:

$$\boxed{\dot{E}_{\mathrm{v}} \;=\; \iint \tfrac{1}{2}\rho\left(v^2 + w^2\right)\; (V_\infty + u)\; d\mathcal{S}_O^{TP}} \tag{40}$$

This is the rate of transverse kinetic energy being deposited in the flow out of the CV. For $u \ll V_\infty, v, w$, this is in fact the same as V_∞ times the induced drag D_i, for the case of a relatively nearby Trefftz Plane where the vortex wake has not yet dissipated significantly.

Wake pressure-defect work rate:

$$\boxed{\dot{E}_{\mathrm{p}} \;=\; \iint (p - p_\infty)\; u\, d\mathcal{S}_O^{TP}} \tag{41}$$

This is the rate of pressure work done of the fluid crossing the Trefftz Plane at some pressure p different from the ambient p_∞.

Wave pressure-work and kinetic energy outflow rate:

$$\boxed{\dot{E}_{\mathrm{w}} = \iint \Big[p - p_\infty + \tfrac{1}{2}\rho\big(u^2 + v^2 + w^2\big)\Big] V_n\; d\mathcal{S}_O^{SC}} \tag{42}$$

This is the pressure work rate and kinetic energy deposition rate of the fluid crossing the Side Cylinder. Normally this will be significant only in supersonic flows, in which the $\dot{E}_{\rm w}$ integrand on $\mathcal{S}_O^{SC}$ is dominated by the oblique wave system, whose integrated contribution to $\dot{E}_{\rm w}$ is equal to the wave-drag power.

For subsonic 3D flows, the $\dot{E}_{\rm w}$ integrand for a lifting wing rapidly decays as $1/r^4$ and hence becomes negligible for a sufficiently distant Side Cylinder. For a relatively nearby Side Cylinder the $\dot{E}_{\rm w}$ integral is nonzero for a subsonic wing, but in this case it merely accounts for the transverse kinetic energy not fully captured in $\dot{E}_{\rm v}$ because of the small Trefftz Plane which accompanies a nearby Side Cylinder.

6 Energy-Outflow Estimation and Characterization

The power balance relation (37), together with the $\dot{E}$ component definitions above, is exact as written, and does not require identification of rotational and irrotational regions over the Trefftz Plane. However, it is useful to briefly identify such regions in order to compare relation (37) to previous force-based analyses.

6.1 Potential-flow regions in low speed flow

Outside of the viscous wakes and propulsion plumes, the pressure defect in low speed flow is given by the Bernoulli relation.

$$\begin{aligned} p - p_\infty &= -\tfrac{1}{2}\rho\left(V^2 - V_\infty^2\right) \\ &= \rho V_\infty u - \tfrac{1}{2}\rho\left(u^2+v^2+w^2\right) \end{aligned} \tag{43}$$

The sum of the three Trefftz Plane $\dot{E}$ components then reduces exactly to the standard induced drag expression times V_∞.

$$\dot{E}_{\rm a}+\dot{E}_{\rm v}+\dot{E}_{\rm p} = \iint \tfrac{1}{2}\rho\left(v^2+w^2-u^2\right) V_\infty \, d\mathcal{S}_O^{TP} \tag{44}$$

$$= D_i \, V_\infty \qquad \text{(pot. flow only)} \tag{45}$$

This sheds further light on the somewhat perplexing $-u^2$ term in the D_i integrand, which seems to run counter to kinetic energy arguments. The negative sign originates from the pressure-work term $\dot{E}_{\rm p}$, which is

negative and twice as large as the true axial kinetic energy loss term $\dot{E}_{\rm a}$. The same pressure-work mechanism was recently identified by Spalart [10] via his entirely different force-based analysis.

6.2 Wave system

For any small-disturbance Mach wave, the following relations can be obtained from oblique-shock theory.

$$p - p_\infty \;=\; -\rho u V_\infty \,-\, \tfrac{1}{2}\rho u^2 M_\infty^2 \tag{46}$$

$$u^2 M_\infty^2 \;=\; u^2 + v^2 + w^2 \tag{47}$$

The $\dot{E}_{\rm w}$ component then becomes

$$\dot{E}_{\rm w} \;=\; \iint -\rho u V_n \, V_\infty \; d\mathcal{S}_O^{SC} \tag{48}$$

$$\;=\; D_w \, V_\infty \tag{49}$$

and as expected, the energy loss rate from the outgoing wave system is simply the power needed to overcome the farfield wave drag.

6.3 Inviscid flow examples – 2D airfoil and 3D wing

For the simple case of an inviscid low-speed 2D airfoil, the perturbation velocities at distances greater than the chord rapidly asymptote to those of a point vortex having the airfoil's circulation Γ. The energy rate integrals can then be readily evaluated for an infinite Trefftz Plane at some location $x > \mathcal{O}(c)$,

$$\dot{E}_{\rm a} \;=\; \frac{\rho V_\infty \Gamma^2}{8\pi} \, \frac{b}{x} \tag{50}$$

$$\dot{E}_{\rm v} \;=\; \frac{\rho V_\infty \Gamma^2}{8\pi} \, \frac{b}{x} \tag{51}$$

$$\dot{E}_{\rm p} \;=\; -\frac{\rho V_\infty \Gamma^2}{4\pi} \, \frac{b}{x} \tag{52}$$

$$\dot{E}_{\rm a} + \dot{E}_{\rm v} + \dot{E}_{\rm p} \;=\; 0 \qquad \text{(2D airfoil)} \tag{53}$$

where b is the arbitrary span of the integration. Although the individual $\dot{E}$ components are quite large near the airfoil due to their $1/x$ behavior, they sum up exactly to zero. This can also be seen from the original

total $\dot{\mathcal{E}}$ definition (34), in which the integrand is zero for this constant total pressure case. This inviscid case also has $\Phi = 0$, so the net required power as given by (37) is zero as well, as expected.

Figure 3 compares the variation of the three Trefftz Plane $\dot{E}$ components (50)–(52) for the 2D airfoil, with the corresponding components for a lifting inviscid 3D wing, the latter integrated numerically for a rigid wake with spanwise elliptical loading.

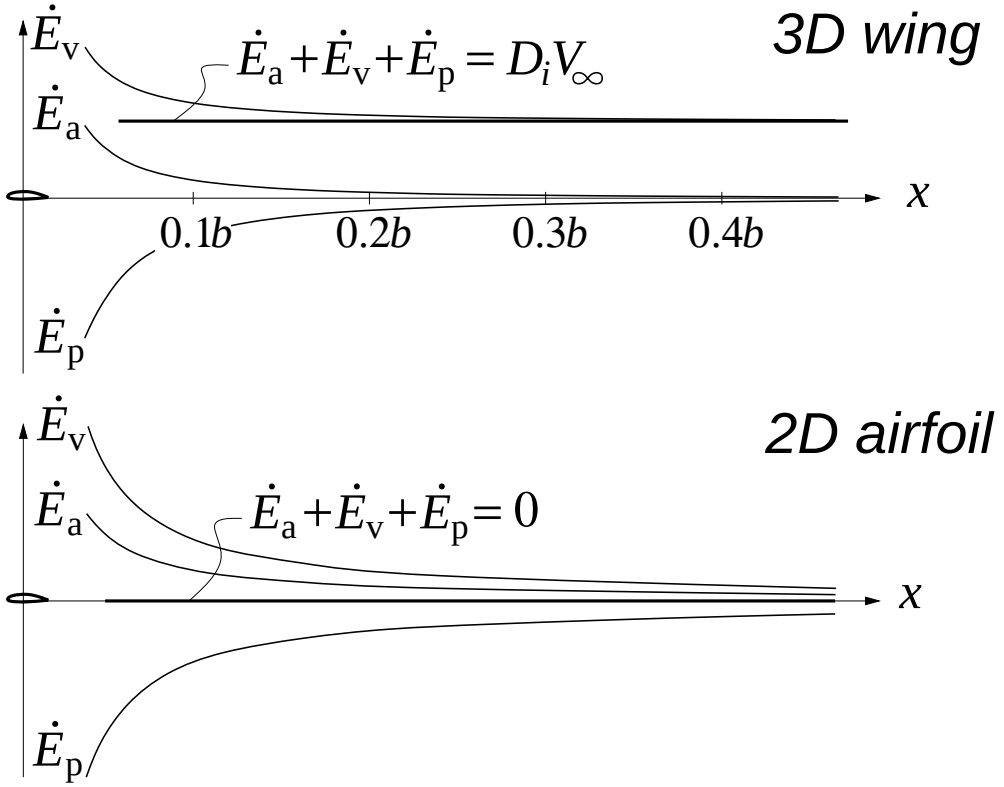

Figure 3: Energy loss rate components versus position of Trefftz Plane, for inviscid 2D airfoil and inviscid 3D wing. For 2D airfoil, the total loss rate is zero. For 3D wing, the total loss rate is constant and equal to $D_i V_\infty$. The individual $\dot{E}_a, \dot{E}_v, \dot{E}_p$ terms asymptote very rapidly in the 3D case.

In the 3D wing case the total energy loss rate is also constant, but equal to $D_i V_\infty$ rather than zero. In 3D the individual $\dot{E}$ components also decay much faster than in the 2D case, with each component very nearly reaching its final value within a fraction of the span b.

$$\dot{E}_a + \dot{E}_v + \dot{E}_p \;=\; D_i V_\infty \;\sim\; \rho V_\infty \Gamma^2 \quad \text{(3D wing)} \tag{54}$$

In the subsequent discussions, these 2D and 3D potential-nearfield "transients" in the individual $\dot{E}_\mathrm{a}, \dot{E}_\mathrm{v}, \dot{E}_\mathrm{p}$ components will be excluded, because they cancel in the overall $\dot{E}$ sum.

6.4 Viscous flow power balance versus Trefftz Plane location

It's important to note that equation (37) holds for any position of the Side Cylinder and Trefftz Plane boundaries, provided Φ is defined as only the dissipation inside the CV. Figure 4 shows how the individual terms in equation (37) vary as the Trefftz Plane is progressively moved downstream.

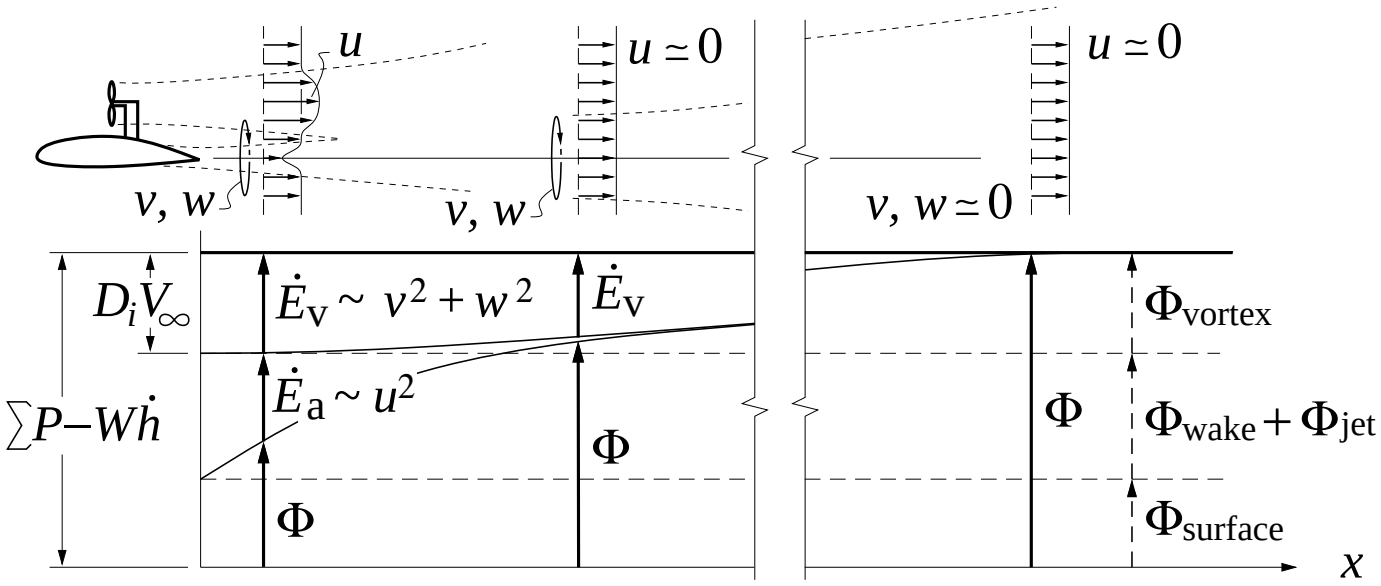

Figure 4: Variation in power balance terms in equation (37), versus position of Trefftz Plane. Transverse velocities of trailing vortices diffuse much later than the axial velocities of propulsors and wakes. Total dissipated power sum is unchanged. The potential-nearfield contributions to $\dot{E}_\mathrm{a}, \dot{E}_\mathrm{v}$ are excluded, $\dot{E}_\mathrm{p}$ is not shown, and $\dot{E}_\mathrm{w}$ is assumed to be zero.

The $\dot{E}_\mathrm{a}$ term defined by (39), intially equal to some fraction of the net axial-force power $F_u V_\infty$, decays relatively quickly as the axial velocity perturbation u decays by mixing and diffusion, with the lost energy appearing as the $\Phi_\mathrm{wake} + \Phi_\mathrm{jet}$ part of the overall dissipation Φ. After a much greater distance downstream the transverse velocities v, w of the trailing vortices also eventually diffuse, and the transverse kinetic energy

integral $\dot{E}_{\rm v}$, initially equal to $D_i V_\infty$, decays accordingly. Again, the dissipation Φ is correspondingly increased by the $\Phi_{\rm vortex}$ part, so that the total power remains unchanged.

7 Dissipation Estimation and Characterization

7.1 Dissipation in Trailing Vortices

As indicated by Figures 2 and 4, all power sources $P_{\scriptscriptstyle P}$,$P_{\scriptscriptstyle V}$,$P_{\scriptscriptstyle K}$ in excess of the potential energy rate $W\dot{h}$ are eventually balanced by the dissipation Φ if the Trefftz Plane is extended sufficiently far downstream. In practice it is advantageous to place the Trefftz Plane close enough so that $\dot{E}_{\rm v} \simeq D_i V_\infty$ contribution from the dissipation of trailing vortices can be kept separate in the power balance in (37). The reason is that D_i can be reliably estimated by other relations, such as the classical result for a planar elliptically-loaded wing without thrust vectoring, for which $F_z = L$.

$$D_i \;=\; \frac{L^2}{\frac{1}{2}\rho V_\infty^2\, \pi\, b^2} \tag{55}$$

Hence, with such alternative $\dot{E}_{\rm v}$ calculation methods being available, $\dot{E}_{\rm v}$ or $\Phi_{\rm vortex}$ do not need to be calculated directly from their definitions.

7.2 Dissipation in Propulsor Jets

The jet dissipation $\Phi_{\rm jet}$ of the isolated propulsor indicated in Figure 2 represents the Froude propulsive (in)efficiency, and hence can be calculated from the disk loading and actuator-disk theory, or from propeller theory, or simply from known propulsor performance.

$$\Phi_{\rm jet} \;=\; P_{\scriptscriptstyle S}\,(1-\eta_{\rm froude}) \tag{56}$$

As with $\Phi_{\rm vortex}$, such alternative models eliminate the need to calculate $\Phi_{\rm jet}$ directly. If (56) is used, then it's simplest to lump it into the left side of equation (37) by replacing $P_{\scriptscriptstyle S}$ with $\eta_{\rm froude} P_{\scriptscriptstyle S}$.

7.3 Dissipation on Propulsor Blading

The Φ_{prop} in Figure 2 represents the dissipation in the propulsor's blading boundary layers, and is otherwise known as "profile losses". This can be computed directly via integration over the blade surface using the dissipation coefficient (discussed later), or by radial blade-element integration using the blade profile drag coefficients, or simply by a known overall profile efficiency if that's available.

$$\Phi_{\text{prop}} \;=\; P_s\,(1-\eta_{\text{profile}}) \tag{57}$$

7.4 Dissipation and Power Loss in Shock Waves

The presence of shock waves will make the various terms in the power balance relation (37) have additional contributions. Figure 5 shows the various shocks which might be present on a transonic or supersonic aircraft. The losses of the nearby strong shocks are best added via the dissipation term Φ, while the losses of the distant waves are best added via the $\dot{E}_{\text{w}}$ term.

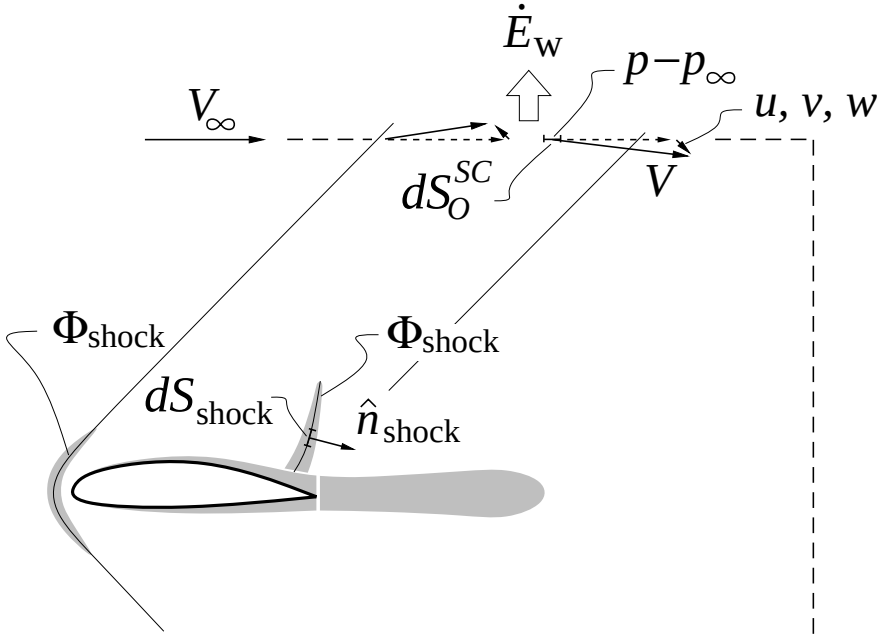

Figure 5: Dissipation in strong shocks near aircraft, and wave pressure-work and kinetic energy outflow through the Side Cylinder.

7.4.1 Nearby strong-shock losses:

The dissipation of a shock is given by

$$\Phi_{\text{shock}} \;\simeq\; \iint \Delta p_t \, \vec{V} \cdot \hat{n}_{\text{shock}} \, d\mathcal{S}_{\text{shock}} \tag{58}$$

where the integration is over the shock surface, with unit normal $\hat{n}_{\text{shock}}$. The total pressure drop Δp_t depends on the normal Mach number $M_\perp$ via standard normal-shock relations.

7.4.2 Outer wave system losses:

The integrand in (58) scales as $\Delta p_t \sim (M_\perp - 1)^3$, which becomes very small as the waves propagate away from the aircraft, where $M_\perp \to 1$. The dissipation therefore requires a great distance to run to completion, and hence is better represented by the $\dot{E}_{\text{w}}$ term in the power balance (37), as discussed previously, and estimated by (48). This $\dot{E}_{\text{w}}$ can be determined by various wave drag D_w estimation methods, such as those of Jones [14] for linearized supersonic flow.

7.5 Dissipation in Shear Layers and Wakes

Since the components of Φ and $\dot{E}$ associated with induced drag, propulsion losses, and shock waves can be expressed or estimated as discussed above, we then only need to consider the remaining dissipation components Φ_{surface} and Φ_{wake}, due to the surface boundary layers and trailing wakes.

For the remainder of the paper we define x, y, z to be the traditional locally-Cartesian shear layer coordinates, where x, z lie on the surface and y is normal to the surface and across the shear layer, as shown in Figure 6. Also, u, w will denote the total x,z velocity components.

The dissipation integrand, which in full contains nine terms, reduces to only two dominant terms in a 3D shear layer, or just one term in a 2D shear layer.

$$\Phi \;=\; \iiint (\bar{\bar{\tau}} \cdot \nabla) \cdot \vec{V} \, d\mathcal{V}$$

$$\simeq \iiint \left(\tau_{xy} \frac{\partial u}{\partial y} + \tau_{zy} \frac{\partial w}{\partial y} \right) dx\, dy\, dz \qquad \text{(3D)} \tag{59}$$

$$\simeq \iiint \tau_{xy} \frac{\partial u}{\partial y}\, dx\, dy\, dz \qquad \text{(2D)} \tag{60}$$

A 2D shear layer is defined as one with a planar velocity profile, or $w = 0$. For brevity in the subsequent discussion, the 2D form will be assumed. The w term can always be added if needed to give the 3D form.

The shear stress consists of the laminar plus turbulent Reynolds stress.

$$\tau_{xy} = \mu \frac{\partial u}{\partial y} - \rho \overline{u'v'} \tag{61}$$

$$\Phi = \iiint \left[\mu \left(\frac{\partial u}{\partial y} \right)^2 - \rho \overline{u'v'} \frac{\partial u}{\partial y} \right] dx\, dy\, dz \tag{62}$$

Since $-\rho \overline{u'v'}$ in conventional shear layers has the same sign as $\partial u / \partial y$, the dissipation integrand is strictly positive, as expected.

7.5.1 Dissipation Coefficient:

For a shear layer, it is convenient to express Φ_{surface}, Φ_{prop}, or Φ_{wake} in terms of a dissipation coefficient $C_{\mathcal{D}}(x, z)$ defined for each point on the shear layer.

$$\Phi = \iint \rho_e u_e^3 C_{\mathcal{D}}\, dx\, dz \tag{63}$$

This is directly analogous to defining friction drag in terms of a skin friction coefficient,

$$D_f = \iint \tfrac{1}{2} \rho_e u_e^2 C_f\, dx\, dz \tag{64}$$

except that $C_{\mathcal{D}}$ is nonzero on a wake.

Using $C_{\mathcal{D}}$ rather than C_f has a number of advantages:

- $C_{\mathcal{D}}$ and Φ capture all drag-producing loss mechanisms. In contrast, C_f and D_f still leave out the pressure-drag contribution.
- $C_{\mathcal{D}}$ and Φ are scalars, so the orientation of the $dx\, dz$ surface element in the (63) integral is immaterial. In contrast, (64) represents a force vector integral, and as written is strictly correct only for flat-plate surfaces aligned with the freestream flow.

- $C_{\mathcal{D}}$ is strictly positive, so there are no force-cancellation problems which often occur with nearfield force integration.

7.5.2 Boundary Layer and Wake Thicknesses

Various shear layer properties can be given in terms of the following integral thicknesses and defects.

$$\text{Mass defect:} \qquad \rho_e u_e\, \delta^* = \int_0^{y_e} (\rho_e u_e - \rho u)\; dy \tag{65}$$

$$\text{Momentum defect:} \quad \rho_e u_e^2\, \theta = \int_0^{y_e} (u_e - u)\, \rho u\, dy \tag{66}$$

$$\text{K.E. defect:} \qquad \rho_e u_e^3\, \theta^* = \int_0^{y_e} \left(u_e^2 - u^2\right) \rho u\, dy \tag{67}$$

$$\text{Density defect:} \qquad \rho_e u_e\, \delta^{**} = \int_0^{y_e} (\rho_e - \rho)\, u\, dy \tag{68}$$

$$\text{Wake K.E. excess:} \quad \rho_e u_e^3\, \delta_{\kappa} = \int_0^{y_e} (u_e - u)^2 \rho u\, dy \tag{69}$$

We also note the following useful identity.

$$\delta_{\kappa} \;=\; 2\theta \;-\; \theta^* \tag{70}$$

Both θ and θ^* obey the von Karman integral momentum equation and the corresponding integral K.E. equation.

$$\frac{d(\rho_e u_e^2 \theta)}{dx} \;=\; \rho_e u_e^2 \frac{1}{2} C_f \;-\; \rho_e u_e \delta^* \frac{du_e}{dx} \tag{71}$$

$$\frac{d(\frac{1}{2}\rho_e u_e^3 \theta^*)}{dx} \;=\; \rho_e u_e^3\, C_{\mathcal{D}} \;-\; \rho_e u_e^2 \delta^{**} \frac{du_e}{dx} \tag{72}$$

The density flux thickness δ^{**} term in (72) represents "ramjet thrust" effects, and is significant only in very high speed or non-adiabatic boundary layers with strong pressure gradients. If this term is negligible, as with most external aerodynamic flows, from (72) we see that in 2D flow of unit span, $\rho_e u_e^3 \theta^*$ at any location measures all the upstream dissipation.

$$\tfrac{1}{2}\rho_e u_e^3 \theta^*(x) \;=\; \int_0^x \rho_e u_e^3 C_{\mathcal{D}}\, dx \;=\; \Phi(x) \tag{73}$$

The various thicknesses can also be used to specify the various integral quantities at the Trefftz Plane,

$$F_u \;=\; \int_{z_{\min}}^{z_{\max}} \rho_e u_e^2 \theta\, dz \tag{74}$$

$$\dot{E}_{\rm a} \;=\; \int_{z_{\rm min}}^{z_{\rm max}} \tfrac{1}{2}\rho_e u_e^3 \delta_K \, dz \tag{75}$$

where the z integration would be over the spanwise extent of the wake.

8 Power Balance in Simple Cases

We now examine the various terms in equation (37) for simple cases, in order to relate these to more familiar drag-related quantities.

8.1 2D Airfoil

In this case we assume that the airfoil is propelled at a steady speed by an isolated ideal propulsor which does not interact with the airfoil's immediate flowfield. The propulsor provides only the thrust T necessary to oppose the drag D (= profile drag in this 2D case). If the ideal propulsor works against the same freestream velocity as the airfoil, it will expend power $P_{\rm isolated} = TV_\infty$ to sustain the thrust. Since there is no induced drag in this 2D flow, equation (37) reads

$$TV_\infty \;=\; P_{\rm isolated} \;=\; \dot{E}_{\rm a} \;+\; \Phi \tag{76}$$

We now choose the Trefftz Plane to be sufficiently far downstream so that $\dot{E}_{\rm a}$ effectively disappears, and we also replace T with D.

$$DV_\infty \;=\; P_{\rm isolated} \;=\; \Phi_{\rm total} \tag{77}$$

Hence, the total dissipation in the flowfield in this case is simply equal to the drag power DV_∞, which is also the power expended by the isolated propulsor.

8.2 2D Airfoil with wake ingestion

This case is the same as above, except that the ideal propulsor is now placed at the airfoil trailing edge, and generates a "perfect" filled-in wake with $u = 0$ everywhere. This is consistent with equation (21), which

indicates a zero net axial force $F_u = 0$ if $u = 0$. We note that in this case $\dot{E}_a = 0$ everywhere, so that the same Φ is obtained for any Trefftz Plane location, and in particular all contributions to Φ occur only on the airfoil surface. Equation (37) then gives the wake-ingesting propulsor power as

$$P_{\text{ingest}} \;=\; \Phi_{\text{surface}} \tag{78}$$

where Φ_{surface} denotes the dissipation occurring in the airfoil surface boundary layers. Note that there is no need to consider or even define "thrust" or "drag", which are not even well-defined for this case. Nevertheless, the propulsive power remains well defined.

It is of particular interest to compare the non-ingesting power from (77) with the ingesting power from (78).

$$P_{\text{isolated}} \;-\; P_{\text{ingest}} \;=\; \Phi_{\text{total}} \;-\; \Phi_{\text{surface}} \tag{79}$$

Referring to Figures 4 or 7, it is evident that this power difference is simply Φ_{wake}, which is the additional Φ contribution of the non-ingested airfoil wake, which is also equal to the kinetic energy flux off the trailing edge.

$$P_{\text{isolated}} \;-\; P_{\text{ingest}} \;=\; \dot{E}_{a_{\text{TE}}} \tag{80}$$

Hence, the benefit of wake ingestion is that it eliminates the downstream dissipation in the wake, equal to $\dot{E}_a$ at that location, which would otherwise occur. For maximum benefit the ingestion must be done at the point of maximum $\dot{E}_a$, which is at or near the trailing edge for most airfoils.

8.3 Flat plate with boundary layer and wake

We now compute the drag on a laminar flat plate of unit span and chord c in three ways, summarized below. In this case the edge velocity $u_e = V_\infty$ is constant, and the surface C_f and $C_{\mathcal{D}}$ coefficients are known in terms of the x-based Reynolds number.

$$\tfrac{1}{2} C_f \;=\; 0.332\,(u_e x/\nu)^{-1/2} \tag{81}$$

$$C_{\mathcal{D}} \;=\; 0.261\,(u_e x/\nu)^{-1/2} \tag{82}$$

1) Skin friction integration.

$$D = \int_0^c \rho_e u_e^2 \, \tfrac{1}{2} C_f \, dx \tag{83}$$

$$= 0.664 \, \rho_\infty V_\infty^2 c \, Re_c^{-1/2} \tag{84}$$

2) Dissipation integration on surface and wake (Trefftz Plane far downstream).

$$DV_\infty = \int_0^c \rho_e u_e^3 \, C_{\mathcal{D}} \, dx \; + \int_c^\infty \rho_e u_e^3 \, C_{\mathcal{D}} \, dx \tag{85}$$

$$= 0.522 \, \rho_\infty V_\infty^3 c \, Re_c^{-1/2} \; + \; \Phi_{\text{wake}} \tag{86}$$

3) Dissipation integration on surface, plus wake kinetic energy flux (Trefftz Plane at trailing edge).

$$DV_\infty = \int_0^c \rho_e u_e^3 \, C_{\mathcal{D}} \, dx \; + \; \left(\tfrac{1}{2} \rho_e u_e^3 \, \delta_K \right)_{x=c} \tag{87}$$

$$= 0.522 \, \rho_\infty V_\infty^3 c \, Re_c^{-1/2} \; + \; \dot{E}_{\text{a}_{\text{TE}}} \tag{88}$$

Relations (86) and (88) are clearly the same, since $\Phi_{\text{wake}} = (\dot{E}_{\text{a}})_{TE}$ as diagrammed by Figure 7. They must also be consistent with (84). Setting the two drag results (84) and (88) equal, we get a numerical value for $(\dot{E}_{\text{a}})_{TE}$, or equivalently for Φ_{wake}

$$0.522 \, \rho_\infty V_\infty^3 c \, Re_c^{-1/2} + \dot{E}_{\text{a}} = 0.664 \, \rho_\infty V_\infty^3 c \, Re_c^{-1/2} \tag{89}$$

$$\dot{E}_{\text{a}} = 0.142 \, \rho_\infty V_\infty^3 c \, Re_c^{-1/2} \tag{90}$$

For the general airfoil case, it may be more convenient to compute or estimate $\dot{E}_{\text{a}}$ using the identity (70),

$$\dot{E}_{\text{a}} = \tfrac{1}{2} \rho_e u_e^3 \delta_K = \rho_e u_e^3 \theta - \tfrac{1}{2} \rho_e u_e^3 \theta^*$$

$$= \tfrac{1}{2} \rho_e u_e^3 \theta^* \left(\frac{2}{H^*} - 1 \right) \tag{91}$$

and an assumed value of H^*, which takes on the following typical narrow range of values.

$$H^* \simeq \begin{cases} 1.50\,, & \text{lam. or turb. separated flow} \\ 1.60\,, & \text{laminar attached flow} \\ 1.75\,, & \text{turbulent attached flow} \end{cases} \tag{92}$$

The trailing edge $\dot{E}_a$ value (90) indicates that for a laminar flat plate, a quite substantial fraction $0.142/0.664 = 21\%$ of the energy losses occur in the wake. This can be seen in Figure 8, which shows the kinetic energy defect $\rho_e u_e^3 \theta^*$ distribution along the plate, which measures the accumulated dissipation via (73). The implication is that an ideal wake-ingesting propulsor for a laminar flat plate could have up to 21% less power consumption than a non-ingesting propulsor.

8.4 2D Airfoil

In the case of an airfoil, the skin friction integration (84) must now be extended to include the pressure drag, and must now be carried into the wake.

$$D = \int_0^c \rho_e u_e^2 \tfrac{1}{2} C_f \, dx + \int_0^\infty -\rho_e u_e \delta^* \frac{du_e}{dx} \, dx \tag{93}$$

In contrast, the dissipation integrals (86) or (88) still have exactly the same form.

$$DV_\infty = \int_0^c \rho_e u_e^3 \, C_{\mathcal{D}} \, dx + \int_c^\infty \rho_e u_e^3 \, C_{\mathcal{D}} \, dx \tag{94}$$

Figure 9 shows the $\rho_e u_e^3 \theta^*$ distributions for the top and bottom surface and wake of a transonic airfoil at high Reynolds number. In this case the wake dissipation is about 13% of the total, which is still large enough to make wake recovery an attractive possibility. The airfoil also has laminar flow up to $x = 0.7$ on the bottom surface, which is responsible for the very low $\rho_e u_e^3 \theta^*$ growth up to that point.

8.5 Dissipation and Skin Friction Coefficients in Shear Layers

8.5.1 Dependence on Shape Parameter, Reynolds Number

The boundary layer shape parameter $H = \delta^*/\theta$ directly indicates the state of the boundary layer, and in particular how close the boundary layer is to separation. Figure 10 shows $C_{\mathcal{D}}$ and $C_f/2$ dependence on H for laminar boundary layers. These scale as $1/Re_\theta$, so the $Re_\theta C_{\mathcal{D}}$ and $Re_\theta C_f/2$ values are independent of Re_θ. Note that the laminar $C_{\mathcal{D}}$ is very nearly independent of H, meaning that laminar boundary layer losses are almost entirely dependent on the Reynolds number, and nearly independent of pressure gradient.

Figure 11 shows the $C_{\mathcal{D}}$ and $C_f/2$ dependence on H for turbulent boundary layers. The $C_{\mathcal{D}}$ now has a clear minimum, close to the H value corresponding to a constant-pressure flow, and increases for both accelerating and decelerating flow. The rapid increase with H essentially represents pressure drag, which in the profile-drag expression (93) is captured by the second term. It should also be noted that the dependence of $C_{\mathcal{D}}$ on Re_θ for turbulent flow is much weaker than the $C_{\mathcal{D}} \sim 1/Re_\theta$ dependence for laminar flow.

The approximate spreading half-angle of 7° observed for a free shear layer [15] implies a dissipation coefficient of approximately

$$C_{\mathcal{D}} \simeq 0.02 \qquad \text{(free shear layer)}. \tag{95}$$

This corresponds to an asymptotic value of $C_{\mathcal{D}}$ for $H \gg 1$ in Figure 11.

8.5.2 Dependence On Flow Velocity

The dissipation expression (63) shows that for any given $C_{\mathcal{D}}$ value, the physical boundary layer losses scale as u_e^3. This implies that "overspeeds", or regions of high local u_e are very costly. Conversely, in regions of low velocity, such as in slat coves which have a fully separated recirculating flow, the losses are quite modest because of the small u_e^3 factor.

8.6 Dissipation-Based Drag Build-Up

The u_e^3 factor in (63) has significant implications for excrescence and interference drag. Traditional excrescence drag estimates, as discussed by Hoerner [16] for example, scale the individual drag contributions with u_e^2, in accordance with a local dynamic-pressure argument. Any discrepancy it typically attributed to some uncertain additional "interference drag". However, (63) clearly shows that a u_e^3 scaling is more appropriate. Furthermore, if no additional dissipation-causing flow structures (e.g. flow separation) are created, there should be no additional uncertain interference drag.

To illustrate the difference between force-based and dissipation-based drag build-up, consider a configuration consisting of a large and a small body, shown in Figure 12. Their relative sizes are such that when

the bodies far apart, the drags are 100 and 1, for a total drag of $D = 101$.

When the small body is placed near the large body where the local velocity is $V_2 = 2$, the force-based drag build-up gives

$$D \;=\; \sum D_k \;=\; 100 + 4 \;=\; 104 \tag{96}$$

while the dissipation-based build-up gives

$$D \;=\; \frac{1}{V_\infty} \sum \Phi_k \;=\; 100 + 8 \;=\; 108 \tag{97}$$

which is a rather different result.

Viscous CFD calculations indicate that the dissipation-based build-up (97) is far more accurate than the force-based build-up (96). The reason is that (96) neglects the additional pressure drag on the large body, due to the potential source flow created by the viscous displacement on the small body. Traditionally this might be labeled "interference drag" of some possibly uncertain origin, but the mechanism and effect is captured quite well by the dissipation-based drag build up (97).

8.7 Evaluation of Alternative Propulsion Systems

The efficiency benefit of wake ingestion is almost universally exploited in marine propulsion, and has also been considered for aeronautical applications. The previous analyses, such as that of Smith [17], have typically computed the propulsor power reduction with the assumption that the ingested airframe boundary layer is given. However, computing or estimating the benefit of integrated/ingesting propulsion systems is far more complex, since the airframe flow is itself modified. An attractive feature of the present energy-based analysis is that comparison of such alternative propulsion systems is considerably simplified, and the competing effects are clearly identified.

Figure 14 shows a traditional isolated propulsor and an alternative integrated propulsor driving a wing. The situation is a more complex version of the one in Figure 7, for two reasons: 1) the integrated propulsor now changes the airframe losses, and 2) there is now an excess thrust for both cases, typically needed to

balance the induced drag and profile drag from other parts of the aircraft. The upper right drawing in Figure 14 shows the "pros", or the loss mechanisms which were eliminated or reduced in switching to the integrated system. These gains consist of removal of the two shear layers and their dissipation, and reduction of the excess wake kinetic energy by filling in of the large upper-surface boundary layer momentum defect. The lower right drawing shows the "cons", or the loss mechanisms which were added in the switch. Quantitative evaluation or estimation of all the pro and con changes shown in Figure 14 would then give the net resulting change in the flight power.

$$\Delta P = \sum \Delta \dot{E} + \sum \Delta \Phi \tag{98}$$

The sums on the righthand side can in principle be carried out to any level of detail deemed appropriate. In addition to the first-level changes shown in Figure 14, one could also account for changes in dissipation Φ_{prof} on the fan blading (e.g. fan profile efficiency), change in the total weight or span loading and resulting change in induced power $\dot{E}_{\text{v}}$, changes in shock losses Φ_{shock} if any, modification to the upper-cowl boundary layer dissipation, etc.

9 Conclusions

A control volume analysis of the flow about an aircraft has been performed, focusing on mechanical energy. The result is a concise relation between all the power sources and sinks in a flowfield, which has a number of useful applications:

- The quantities which directly influence flight power requirements are clearly identified.
- It is fully consistent with previous analyses based on momentum.
- There is no need to define the rather ambiguous "thrust" or "drag" in configurations with tightly integrated propulsion systems.
- The wake energy loss is clearly decomposed into independent contributions due to axial and transverse wake velocities, without the need to separately identify treat rotational and irrotational regions of

the Trefftz-Plane. This eliminates the ambiguity between thrust, profile drag, and induced drag in configurations where the viscous wakes and the vortex wakes are not distinct.

- For traditional drag build-up analyses, using the power approach appears to be more reliable in that it accounts for interference effects which are not captured by the force approach.

The author would like to thank one of the reviewers for the suggestions to examine the issue of unsteady flows, and the energy-term cancellations in the 2D inviscid airfoil case.

References

[1] A. Betz. Ein verfahren zur direkten ermittlung des profilwiderstandes. *ZFM*, 16:42–44, Feb 1925.

[2] B. Jones. Measurement of profile drag by the pitot-traverse method. R & M Report 1688, Aeronautical Research Council, 1936.

[3] K. Oswatisch. Der verdichtungsstoss bei der stationären umströmung flacher profile. *ZAMM*, 29:129–141, 1949.

[4] E.C. Maskell. Progress towards a method of measurement of the components of the drag of a wing of finite span. Technical Report 72232, Royal Aircraft Establishment, Jan 1973.

[5] I. Kroo. Drag due to lift: Concepts for prediction and reduction. *Annual Reviews of Fluid Mechanics*, 33:587–617, 2001.

[6] C. VanDam. Recent experience with different methods of drag prediction. *Progress in Aerospace Sciences*, 35:751–798, 1999.

[7] M.B. Giles and R.M. Cummings. Wake integration for three-dimensional flowfield computations: Theoretical development. *Journal of Aircraft*, 36(2):357–365, 1999.

[8] K. Kusunose. *A Wake Integration Method for Airplane Drag Prediction.* Tohoku University Press, Sendai, Japan, 2005.

[9] M. Méheut and D. Bailly. Drag-breakdown methods from wake measurements. *AIAA Journal*, 46(4):847–862, 2008.

[10] P.R. Spalart. On the far wake and induced drag of aircraft. *Journal of Fluid Mechanics*, 603:413–430, 2008.

[11] J.D. Denton and N.A. Cumpsty. Loss mechanisms in turbomachinery. IMechE Paper C260/87, 1987.

[12] J.D. Denton. Loss mechanisms in turbomachinery. *Journal of Turbomachinery*, 115, Oct 1993.

[13] E.M. Greitzer, C.S. Tan, and Graf M.B. *Internal Flow — Concepts and Applications*. Cambridge University Press, Cambridge, 2004.

[14] R.T. Jones. *Wing Theory*. Princeton University Press, Princeton, NJ, 1990.

[15] F.M. White. *Viscous Fluid Flow*. McGraw-Hill, New York, 1974.

[16] S.F. Hoerner. *Fluid-Dynamic Drag*. Hoerner Fluid Dynamics, Vancouver, WA, 1965.

[17] L.H.Jr. Smith. Wake ingestion propulsion benefit. *Journal of Propusion and Power*, 9(1):74–82, Jan–Feb 1993.

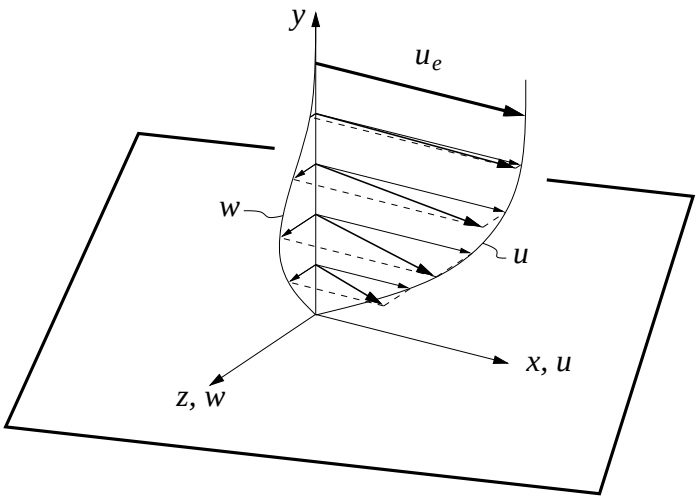

Figure 6: Boundary layer profile on surface, with locally-cartesian x, y, z axes. The x-axis is defined to lie along edge velocity u_e.

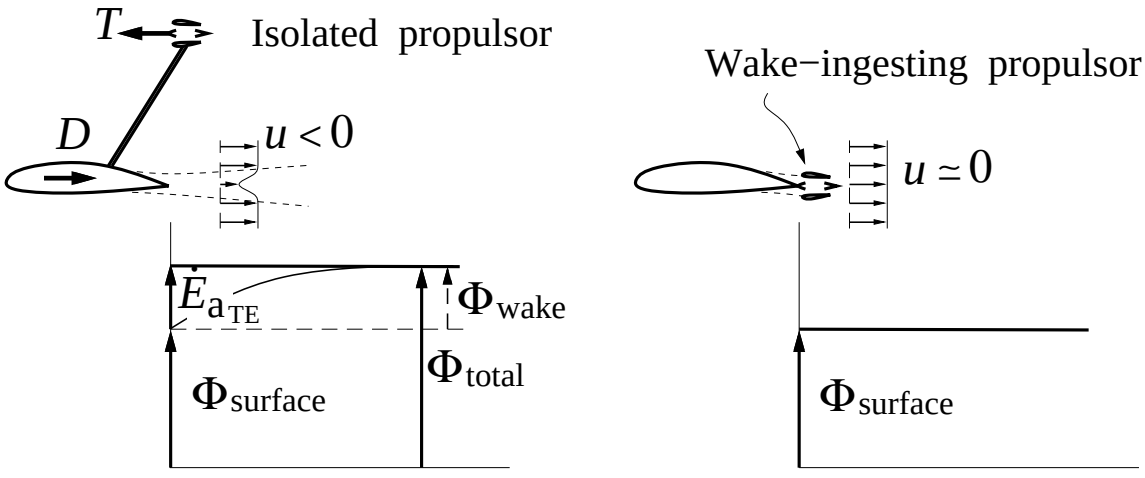

Figure 7: Comparison of dissipation in isolated and wake-ingesting propulsors for 2D airfoil.

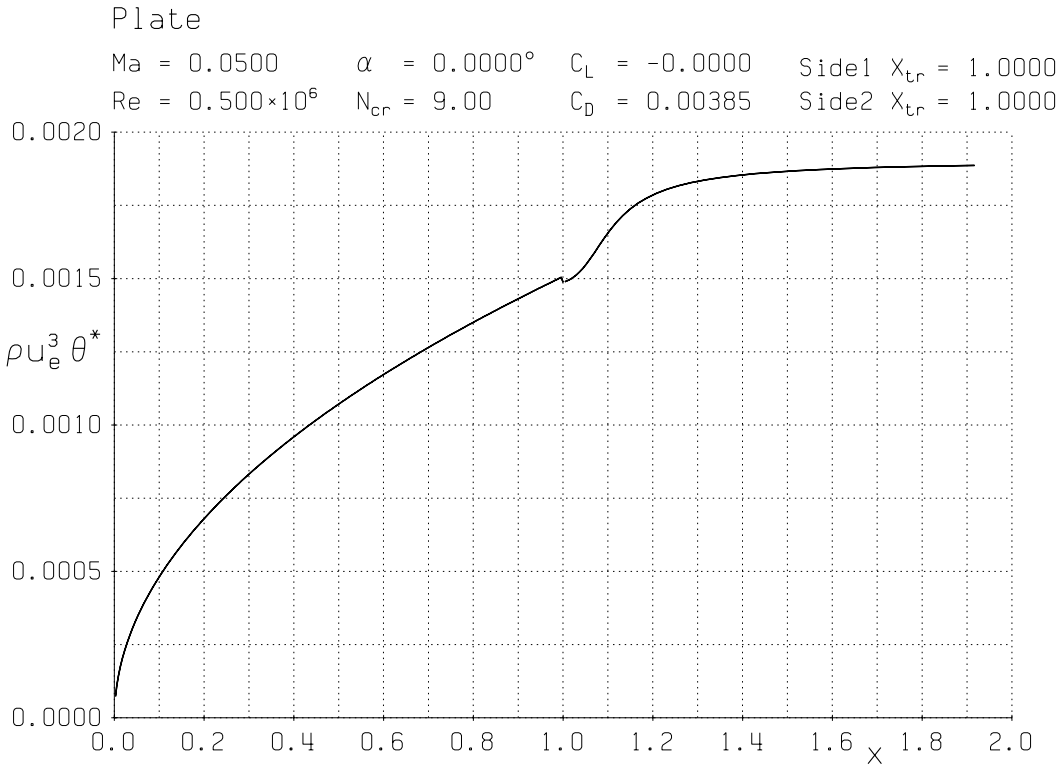

Figure 8: Kinetic energy defect $\rho_e u_e^3 \theta^*$ distribution on a laminar flat plate. This shows the accumulating dissipation on the surface, and in the wake which starts at $x=1$.

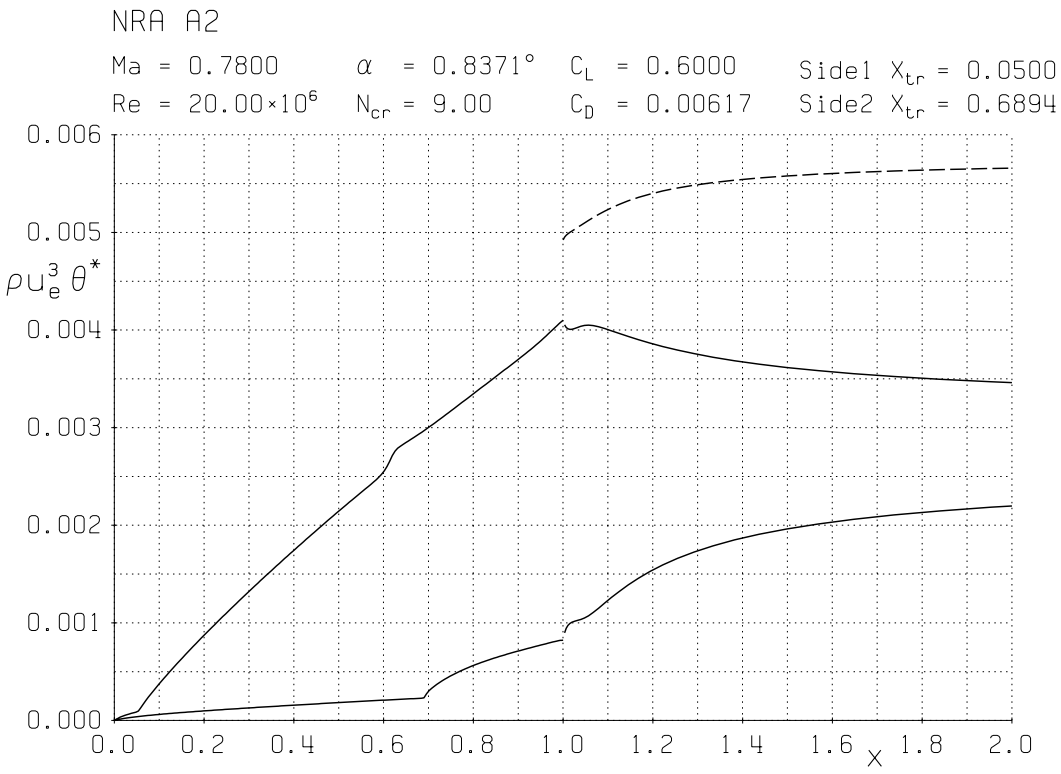

Figure 9: Transonic airfoil $\rho_e u_e^3 \theta^*$ distributions on top and bottom surfaces and wake halves, and for wake total (dashed line).

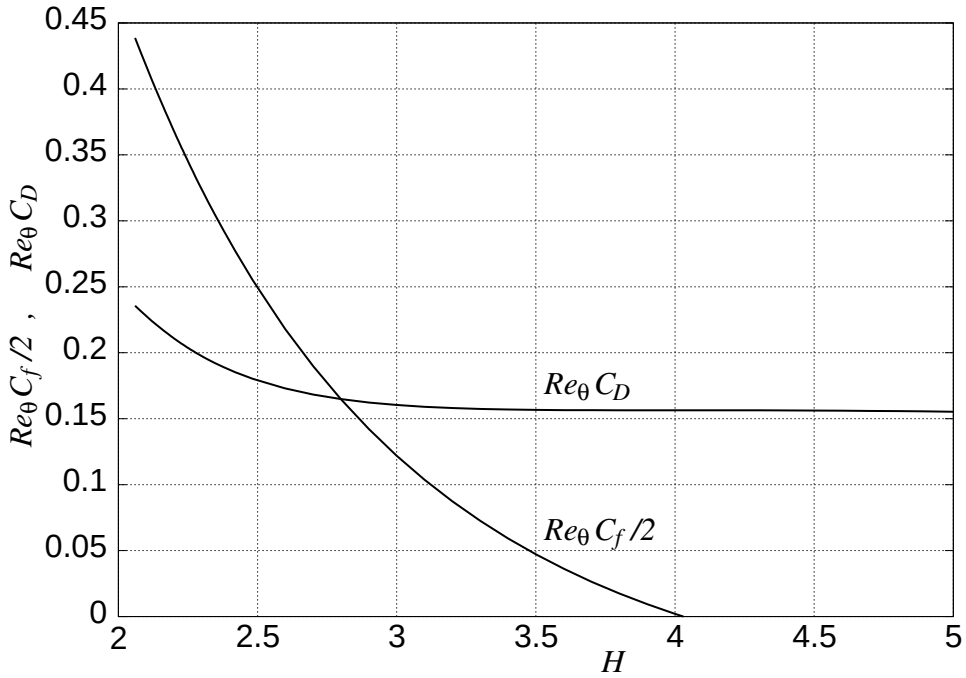

Figure 10: $Re_\theta C_{\mathcal{D}}$ and $Re_\theta C_f/2$ versus H for laminar boundary layers.

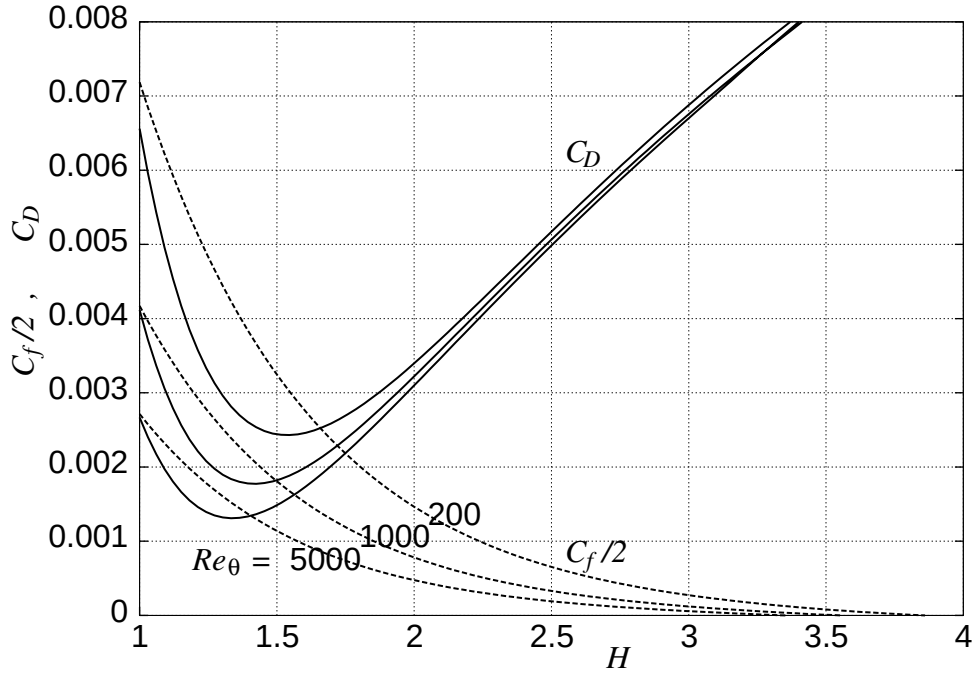

Figure 11: $C_{\mathcal{D}}$ and $C_f/2$ versus H for turbulent boundary layers, for $Re_\theta = 200, 1000, 5000$.

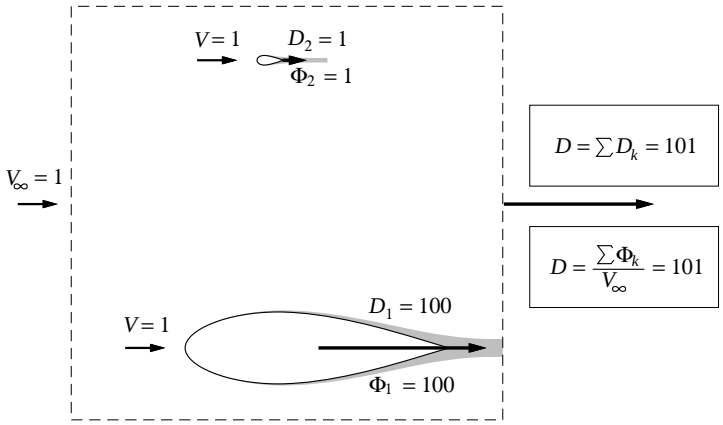

Figure 12: Drag build-up for two isolated bodies by force summation (top box), and dissipation summation (bottom box).

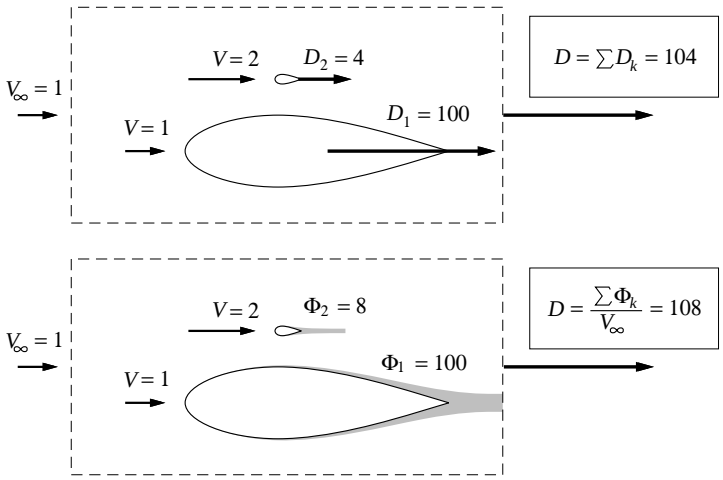

Figure 13: Drag build-up for two closely interacting bodies by force summation (top), and dissipation summation (bottom). The small body is in the large body's nearfield, and sees a doubled local velocity.

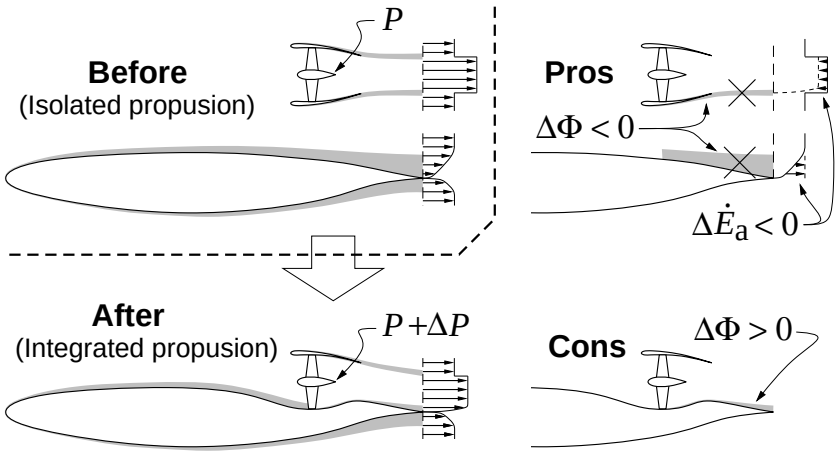

Figure 14: Changes resulting from switch from isolated to distributed propulsion, while keeping the same net streamwise momentum defect and force. Power change ΔP is the net result of negative (pro) and positive (con) $\Delta\Phi$ and $\Delta\dot{E}$ changes.